Analysis of High-Reynolds-Number Lid-Driven Cavity Flow Using Enhanced Dynamic Mode Decomposition

Ping Wang(王平)[1], Huisong Bai(白辉松)[1], Yong Peng[2,*](彭勇), Jianguo Zhou[3](周建国) , Guangyao Xu[1](许光耀), Yuji Peng[1](彭宇骥)

[1] College of Water Resources and Architectural Engineering, Northwest A&F University, Yangling, Shaanxi 712100, China. Email:1179424728@foxmail.com

[2] College of Water Resources and Architectural Engineering, Northwest A&F University, Yangling, Shaanxi 712100, China. Email: pengyongscu@foxmail.com

[3]Department of Computing & Mathematics, Manchester Metropolitan University, Manchester M1 5GD, UK, Email: J.Zhou@mmu.ac.uk

* Corresponding author: Yong Peng, pengyongscu@foxmail.com

Abstract:

To address the challenge of modal characterization of complex turbulent structures in high Reynolds number cavity flow, this study integrates the Time Integration Contribution - Dynamic Mode Decomposition (TIC-DMD) and Sparsity-Promoting Dynamic Mode Decomposition (SPDMD) as multi-scale analysis methods. Utilizing Particle Image Velocimetry (PIV) experimental data (Re=5×10^5 and Re=2×10^6), it comprehensively analyzes the dynamic characteristics and modal reconstruction performance of high Reynolds number cavity flow. The findings show that the TIC-DMD effectively extracts the dominant vortex structures through a time-domain energy integration mechanism. At Re = 5×10^5, it achieves 61.02% reduction in reconstruction error compared to SPDMD when using a high modal number (N=246), significantly enhancing its ability to capture multi-scale turbulence. In addition, the SPDMD suppresses noise interference through sparsity constraints, achieving a reconstruction error of 0.0593 with a low modal number (N=7), a 75.79% improvement over the standard DMD. Both methods' first-order modes consistently stably reconstruct the dominant vortex structures of the flow field, while the standard DMD suffers from

mode fragmentation due to noise sensitivity. Further analysis reveals that SPDMD excels at low modal numbers, whereas TIC-DMD offers superior stability and accuracy in flow field reconstruction as the modal number increases, particularly for high Reynolds number flows. The modal analysis framework developed in this study introduces a novel paradigm for modeling complex flows. The framework proposes to integrate experimental data with the Large Eddy Simulation (LES) benchmark database, thereby advancing engineering applications in high Reynolds number flow control.

Keywords: High Reynolds number cavity flow; Dynamic Mode Decomposition; TIC-DMD; SPDMD; Multi-scale turbulence

1. Introduction

With the rapid development of Computational Fluid Dynamics (CFD) and experimental techniques, investigating the spatiotemporal evolution and underlying mechanisms of complex flow fields has become an increasingly critical focus in modern fluid mechanics research. In particular, when studying high Reynolds number flows, the intricate turbulence characteristics and multi-scale structures significantly increase the difficulty of analyzing their dynamic behavior and flow mechanisms. Conventional dimensionality reduction techniques, such as Proper Orthogonal Decomposition (POD) and Dynamic Mode Decomposition (DMD), encounter significant challenges in handling turbulence, especially due to the dominance of nonlinear interactions that drive dynamic complexity (Roy et al.,2023; Mohan et al.,2018). The optimal linear bases of these methods fail to adequately capture such complexities (Schmid 2010; Rowley et al., 2009). High Reynolds number flows are typically characterized by pronounced nonlinear and unsteady phenomena, including three-dimensional turbulence structure (Marusic & Monty, 2019; Smits et al., 2021), vortex formation and evolution (Haller, 2015; Green et al., 2020), and flow field instability phenomena (Taira et al., 2017; Schmid, 2022). These characteristics pose substantial challenges for the analysis and prediction of high Reynolds number flow fields in fluid mechanics research (Menon & Mittal 2020).

DMD, initially proposed by Schmid et al. (2010), aims to extract dynamic modes of the flow field from experimental or numerical simulation data. This method is fundamentally based on the Koopman operator theory, which maps a nonlinear system onto an infinite-dimensional linear space. By identifying a set of low-dimensional subspaces as bases, DMD describes the evolution of the flow field through the superposition of these subspaces in a new low-dimensional coordinate system (Kou et al.,2018; Tiziano et al.,2022). It successfully captures the key dynamic characteristics of the flow field such as vortex structures, dominant frequencies, and growth rates by identifying and extracting them. As research has advanced, data-driven analysis methods have gradually become an essential tool for feature extraction and reduced-order modeling of complex flow fields (Marensi et al.,2023). As an emerging modal analysis technique, DMD decomposes time-series data into modes and eigenvalues, revealing the key dynamic characteristics of the flow field (Ming et al.,2020). This method has been widely applied to various classical flow problems, such as turbulence analysis (Rowley et al.,2009), vortex street characteristics (Ye et al., 2017), and flow field reconstruction in aerospace and wind tunnel experiments (Mohan & Gaitonde 2017).

However, studies have shown that standard DMD is sensitive to noise interference and struggles to effectively identify dominant modes in complex systems (Feldhusen et al.,2021; Hemati et al.,2017). Additionally, in high Reynolds number flows, both the accuracy of mode selection and computational efficiency require improvement (Chávez-Dorado et al.,2025). To address these issues, Jovanović et al. (2014) proposed the Sparsity-Promoting Dynamic Mode Decomposition (SPDMD) method. SPDMD enhances mode selection accuracy by introducing sparsity constraints, which optimize modal amplitude vectors, retain important modes, and reduce noise interference. Moreover, Tsolovikos et al. (2020) applied SPDMD to estimation and control in complex flow environments, demonstrating its robustness in fluid system control (Jovanović et al., 2014). Hu et al. (2023) validated the efficiency of SPDMD in turbine flow field prediction, providing a fast and effective tool for turbine mechanical design

(Li et al.,2022).

Furthermore, standard DMD modal ordering is usually based on initial energy or growth rate(Kong et al.,2020). However, in high Reynolds number flows, multi-scale characteristics result in time-dependent evolution of modal importance (Kutz et al.,2016). Consequently, accurately assessing mode importance requires considering both initial conditions and global evolution characteristics. To address this, Kou et al. (2016) proposed the TIC method, which ranks modes by integrating their accumulated energy over the entire time domain. This approach significantly improves sensitivity to mode convergence and initial conditions (Asada et al.,2025).

At low Reynolds numbers, the dominant frequency is relatively clear, whereas the multi-scale characteristics and broad frequency spectrum of high Reynolds number flows make mode selection more complex (Baars et al.,2017). Although DMD has achieved remarkable results in turbulence, vortex street, and unsteady flow analysis (Brunton et al., 2020; Abu & Sung. 2011; Li et al., 2017; Li et al.,2021), research on cavity flows has primarily focused on low to moderate Reynolds numbers (Burggraf et al., 1966; Koseff & Street, 1984; Gustafson & Halasi, 1987;Chen et al., 2014; Tanase, et al.,2017;Wang et al.,2025). Studies on high Reynolds number ($Re \geq 1\times10^5$) cavity flows remain limited, particularly regarding the precise modal extraction using DMD methods. This paper applies TIC-DMD and SPDMD methods for modal decomposition and flow field reconstruction. By comparing the differences in mode selection, eigenvalue spectra, frequency-energy spectra, and flow field reconstruction errors between the two methods, this study not only reveals the dynamic characteristics of high Reynolds number flow fields but also provides reliable benchmark data for LES/Direct Numerical Simulation (DNS) turbulence models through physical experiments of high Reynolds number cavity flow. Additionally, the findings enhance theoretical understanding of TIC-DMD and SPDMD methods in high Reynolds number flows, supporting both research and engineering applications in fluid dynamics.

2. Research Methods and Data Essentials

This study combines TIC-DMD and SPDMD methods to extract the main dynamic characteristics of the flow field and construct reduced-order models based on high Reynolds number flow field data. This section provides a detailed explanation of the DMD method, data sources, snapshot construction, and modal sorting methods, among others.

2.1 Dynamic Mode Decomposition Method

DMD is a mathematical method used to extract dynamic information of the flow field from experimental data or numerical simulations (Nguyen et al., 2023). It reduces the dimensionality of the flow field data, revealing the main dynamic characteristics of the system (Kou & Zhang, 2016), and provides reduced-order modeling for complex flow behaviors. For flow field data from time t_1 to t_N, the flow field snapshots can be represented as:

$$V_1^N = \{v_1, v_2, v_3, \ldots, v_N\} \tag{1}$$

here, v_i represents the flow field snapshot at the *i*-th time step, with a time interval of Δt. Assuming that the system can be described by a discrete linear dynamical system, the relationship can be written as:

$$Y = AX \tag{2}$$

where:

$$Y = \{v_2, v_3, \ldots, v_N\} = V_2^N \tag{3}$$

$$X = \{v_1, v_2, \ldots, v_{N-1}\} = V_1^{N-1} \tag{4}$$

The system matrix A can shift the physical field along the time dimension by Δt, thus the eigenvalues of A characterize the time evolution properties of V_1^N.

Since the snapshot matrices X and Y of the flow field typically have high-dimensional features, the system matrix A contains a large amount of data. As a result, it is necessary to extract the eigenvalues using the reduced-order matrix $\tilde{A}$. The core of DMD is to reduce the dimensionality of the flow field through a similarity transformation method combined with Singular Value Decomposition (SVD), ensuring numerical stability while obtaining a low-dimensional dynamical description of the system (Liao, 2023).

Through the POD method, the relationship between A and its reduced-order matrix $\tilde{A}$ can be expressed as:

$$A = U\tilde{A}U^{*} \tag{5}$$

here, U is the left singular matrix obtained from the SVD of the snapshot matrix X:

$$X \approx U\Sigma V^{*} \tag{6}$$

By substituting equations (2) and (4) into (3), the expression for the reduced-order matrix is obtained:

$$\tilde{A} = U^{*}YV\Sigma^{-1} \tag{7}$$

in which $\tilde{A}$ is the optimal low-dimensional estimate matrix of A. By solving for the eigenvalues and eigenvectors of $\tilde{A}$, the DMD analysis results can be obtained. Performing an eigenvalue decomposition on matrix $\tilde{A}$:

$$\tilde{A} = Q\lambda Q^{-1} \tag{8}$$

where the j-th eigenvalue of $\tilde{A}$ is λ_j, and the corresponding eigenvector is Q_j. The j-th DMD mode can be defined as:

$$\Phi_j = UQ_j \tag{9}$$

The modulus and phase of the eigenvalue represent the growth rate g_j and frequency w_j (Hz) of the mode, respectively:

$$g_j = \frac{\mathrm{Re}\{\log(\lambda_j)\}}{\Delta t} \tag{10}$$

$$w_j = \frac{\mathrm{Im}\{\log(\lambda_j)\}}{2\pi\Delta t} \tag{11}$$

The flow field snapshot at any time can be approximated as:

$$v_i = Av_{i-1} = U\tilde{A}U^{*}v_{i-1} = UQ\lambda Q^{-1}U^{*}v_{i-1} = UQ\lambda^{i-1}Q^{-1}U^{*}v_1 \tag{12}$$

Each column of Φ is defined as the corresponding DMD mode in space. From equation (7), we have:

$$\Phi = UQ \tag{13}$$

The initial amplitude of the mode is defined as:

$$\alpha = Q^{(-1)}U^{*}v_1 \tag{14}$$

here, α represents the contribution of this mode to the initial snapshot v_1, and $U^{*}v_1$ represents the new system constructed corresponding to the first snapshot flow field. At this point, the flow field snapshot v_i is expressed as:

$$v_i = \Phi\lambda^{i-1}\alpha = \sum_{j=1}^{r}\Phi_j\lambda_j^{i-1}\alpha_j = \sum_{j=1}^{r}\Phi_j e^{\frac{\log(\lambda_j)}{\Delta t}*t}\alpha_j \tag{15}$$

where Φ_j represents the *j*-th mode value, λ_j^{i-1} is the eigenvalue of the *j*-th mode at the i−1-th time step, and α_j is the amplitude of the *j*-th mode. Through this method, the temporal evolution of the flow field can be effectively predicted.

2.2 Sparsity-Promoting Dynamic Mode Decomposition

SPDMD is an extended method of standard DMD that introduces sparsity constraints (Schmid et al.,2023). SPDMD optimizes the modal amplitude vectors by retaining only the most representative modes, reducing noise, and improving the accuracy of mode selection. This method effectively highlights the main dynamic features of the system while minimizing interference from redundant modes (Pasquariello et al.,2017).

2.2.1 Sparse Structure Selection

From equation (13), the approximate form of the flow field snapshot matrix can be obtained:

$$X \approx \Phi H V_{and} \tag{16}$$

$$= \left[\oint_1 \cdots \oint_i\right]\begin{pmatrix} \alpha_1 & 0 & \cdots & 0 \\ 0 & \alpha_2 & \cdots & 0 \\ \vdots & \vdots & \ddots & \vdots \\ 0 & 0 & \cdots & \alpha_i \end{pmatrix}\begin{pmatrix} 1 & \lambda_1 & \cdots & \lambda_1^{N-2} \\ 1 & \lambda_2 & \cdots & \lambda_2^{N-2} \\ \vdots & \vdots & \ddots & \vdots \\ 1 & \lambda_m & \cdots & \lambda_i^{N-2} \end{pmatrix} \tag{17}$$

in which, H is the initial amplitude coefficient matrix, and V_{and} is the Vandermonde matrix containing oscillatory mode information.

To extract the key oscillatory information of the system, the modal amplitude α_i needs to be precisely estimated through an optimization problem. The goal is to minimize the reconstruction error, and the Frobenius norm approximation of the problem is expressed as (Chen et al.,2014):

$$\begin{aligned} \min J(\alpha) &= \| X - \phi H V_{\text{and}} \|_F^2 \\ &= \text{tra}\left(\left(\Sigma V^* - Q H V_{\text{and}}\right)^* (\Sigma V^* - Q H V_{\text{and}})\right) \\ &= \alpha^* P \alpha - q^* \alpha - \alpha^* q + s \end{aligned} \tag{18}$$

To minimize $J(\alpha)$, we obtain:

$$\alpha = P^{-1} q = ((Q^* Q) \cdot (V_{\text{and}} V_{\text{and}}^*))^{-1} \overline{\text{diag}(V_{\text{and}} V \Sigma^* Q)} \tag{19}$$

We address the sparsity-inducing problem by enhancing the objective function $J(\alpha)$ with additional content. This penalty seeks to reduce the number of non-zero elements in the unknown amplitude vector:

$$\underset{\alpha}{minimize}\; J(\alpha) + \gamma \sum_{i=1}^{r} |\alpha_i| \tag{20}$$

here, γ>0 is the sparsity regularization parameter, controlling the strength of the sparsity constraint, and α_i represents the absolute value of the amplitude of the *i*-th mode. As γ increases, the number of non-zero elements in α gradually decreases, thus achieving sparse structure selection.

To solve the above convex optimization problem, the Alternating Direction Method of Multipliers (ADMM) is used. The specific steps are as follows:

①Replace the amplitude vector α with a new variable β. The optimization problem in equation (20) is converted into the following constrained optimization problem:

$$\begin{aligned} &\text{minimize } J(\alpha) + \gamma g(\beta) \\ &\text{subject to } \alpha - \beta = 0. \end{aligned} \tag{21}$$

here, $g(\beta) = \sum_{i=1}^{r} |\beta_i|$, and equation (21) is equivalent to equation (20).

②Introduce the augmented Lagrangian function to convert the constraint in equation (21) into an objective function:

$$L_{\rho}(\alpha,\beta,\lambda) := J(\alpha) + \gamma g(\beta) + \frac{1}{2}(\lambda^{*}(\alpha-\beta) + (\alpha-\beta)^{*}\lambda + \rho\|\alpha-\beta\|_2^2) \tag{22}$$

where θ is the Lagrange multiplier, and $\rho>0$ is the penalty parameter, controlling the weight of the constraint term.

③Minimize over α, minimize over β, and update the Lagrange multiplier:

$$\begin{aligned} \alpha^{k+1} &:= \arg L_{\rho}(\alpha, \beta^{k}, \lambda^{k}), \\ \beta^{k+1} &:= \arg L_{\rho}(\alpha^{k+1}, \beta, \lambda^{k}), \\ \lambda^{k+1} &:= \lambda^{k} + \rho(\alpha^{k+1} - \beta^{k+1}). \end{aligned} \tag{23}$$

④Begin iterations from the initial point (β_0, θ_0) and solve until the following error condition is met:

$$\begin{aligned} &\|\alpha^{k+1} - \beta^{k+1}\|_2 \le \epsilon_{\text{prim}} \\ &\|\beta^{k+1} - \beta^{k}\|_2 \le \epsilon_{\text{dual}} \end{aligned} \tag{24}$$

2.2.2 Amplitude Correction

After sparse structure selection, SPDMD further corrects the amplitude to balance the reconstruction quality and the number of modes (Arai et al.,2021). With the sparse structure fixed, only the non-zero amplitudes are optimized through the following convex optimization problem:

$$\begin{aligned} &\text{minimize} \quad J(\alpha) \\ &\text{subject to} \quad E^{T}\alpha = 0 \end{aligned} \tag{25}$$

here, E is the encoding matrix used to constrain the sparse structure of the non-zero modes. Its columns are unit vectors, and E encodes the sparse structure information of the amplitude α.

①Introduce the Lagrangian function:

$$\begin{gathered} L(\alpha,\nu) = J(\alpha) + \nu^{*}E^{T}\alpha + (E^{T}\alpha)^{*}\nu \\ \begin{bmatrix} P & E \\ E^{T} & 0 \end{bmatrix} \begin{bmatrix} \alpha \\ \nu \end{bmatrix} = \begin{bmatrix} q \\ 0 \end{bmatrix} \end{gathered} \tag{26}$$

②The corrected sparse amplitude vector α_{sp} is obtained:

$$\alpha_{\mathrm{sp}} = [I\ 0]\begin{bmatrix} P & E \\ E^T & 0 \end{bmatrix}^{-1}\begin{bmatrix} q \\ 0 \end{bmatrix} \tag{27}$$

2.3 Data Description and Snapshot Construction

The velocity distribution in the middle plane has long been a focal point in the analysis of cavity flow, both in experiments and numerical studies. Thus, this study selects the middle plane of a square cavity for flow field measurements. The experimental data were collected using a PIV system, with measurements conducted in a 0.5-meter square cavity at Reynolds numbers of 5×10^5 and 2×10^6. To improve measurement accuracy, a high-speed camera (resolution: 1920×1080 pixels, maximum frame rate: 1000 fps) and an 8W laser (wavelength: 532 nm) were employed. The tracer particles used were hollow glass microspheres with a particle size of 10μm. Prior to measurements, the conveyor belt was run for 10 to 15 minutes to stabilize the flow pattern. Tracer particles were then evenly distributed within the fluid to ensure uniform distribution under laser illumination. The laser was activated and adjusted to an appropriate intensity to ensure uniform illumination of the target area. After starting the high-speed camera, the capture frequency, exposure time, and acquisition duration were set, and the flow field image data were captured and saved using dedicated acquisition software.

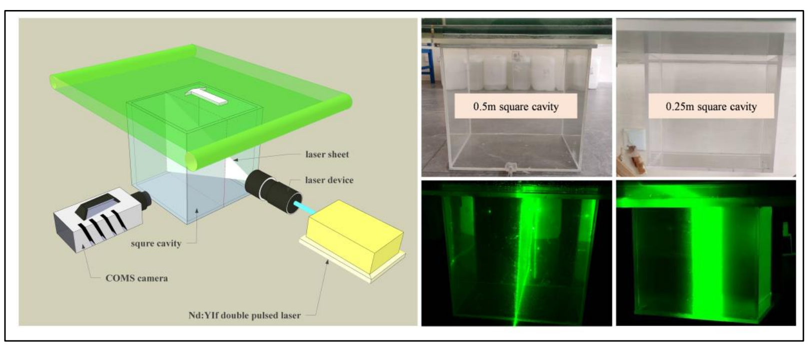

Figure1. Lid-driven cavity

2.4 Modal Sorting Methods for Two Dynamic Mode Decomposition Approaches

In DMD method, modal sorting remains a critical issue. Common sorting methods include modal norm methods, initial amplitude methods, and frequency-weighted methods (Peng et al., 2022). To more accurately assess the importance of modes, this study adopts TIC-DMD method, which measures each mode’s contribution to the entire dataset by calculating the integral of the absolute value of the time coefficient for each mode. TIC-DMD provides a comprehensive reflection of the mode's importance, is suitable for periodic and linear flows, and is also effective for analyzing unstable or transient systems (Li et al., 2024).

The energy modal index is defined as:

$$I_j = \int |b_j(t)|\, dt \approx \sum_{i=1}^{N} |b_{ij}|\, dt \tag{28}$$

where I_j represents the energy index of the *j*-th mode, and $b_j(t)$ is the time coefficient of the mode as it varies over time. The time integral measures the energy contribution of the mode across the entire data sequence. Compared to standard methods, this index provides a more stable and accurate modal sorting criterion.

For SPDMD, the modal energy sorting is based on the corrected modal amplitude values. The SPDMD method, through sparsity optimization, retains only a few key modes, thereby improving the accuracy of mode selection and reducing interference from noise.

3.Results and Discussion

3.1 Modal Selection and Reconstruction Error Analysis

In both TIC-DMD and SPDMD methods, modal selection is a key factor influencing the flow field reconstruction accuracy and dynamic feature extraction. TIC-DMD typically relies on energy sorting to manually select the number of modes, while SPDMD optimizes the number of modes automatically by introducing a sparsity regularization parameter γ and a loss function (Wang et al., 2022). Although both methods require the specification of the number of modes, TIC-DMD determines the number of modes through energy sorting, whereas SPDMD selects the number of modes by optimizing the loss function. For comparison purposes, the number of modes was set to seven in both methods in this study. Considering the impact of conjugate modes, four independent modes were extracted in practice.

To investigate the convergence of the SPDMD method with varying modal numbers, the loss function $\mathcal{V}_{\text{loss}}$ (Pasquariello et al., 2017) is defined as:

$$\mathrm{V}_{\text{loss}} = 100\sqrt{\frac{J(\alpha)}{J(0)}} = 100\frac{\| X - \phi H V_{\text{and}} \|_F^2}{\| X \|_F} \tag{29}$$

Figure 2 shows the relationship between the SPDMD penalty coefficient γ and the number of modes at different Reynolds numbers. As γ increases, the number of modes gradually decreases, indicating that the sparsity constraint effectively compresses the redundant modes. However, even at higher values of γ, the number of modes remains above 100, suggesting that the complex dynamic features of the flow field have not been fully compressed. The Reconstruction Error rate initially increases sharply before stabilizing as the number of modes decreases, remaining relatively high value of around 15% or more. This indicates that the method struggles to fully capture the multi-scale characteristics of high Reynolds number flow fields, where nonlinear behaviors become more pronounced and mode coupling effects intensify, reducing modal sorting accuracy. Moreover, DMD methods inherently rely on linear system approximations, which inherently limit their ability to fully represent the nonlinear dynamical characteristics of real-world flow fields. This limitation can lead to discrepancies between extracted modes and the physical reality of the flow, further compromising modal fidelity (Gosea & Pontes Duff, 2021). Additionally, noise from the PIV measurement system further degrades the fidelity of flow field representation (Liu *et al.*, 2020).

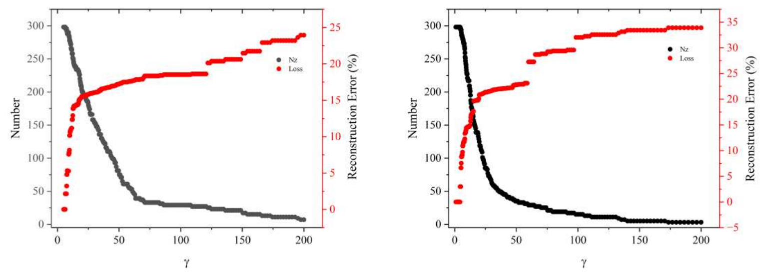

(a) Re=5×10^5 (b) Re=2×10^6

Figure 2: SPDMD - Penalty Coefficient γ, Number of Modes , Reconstruction Error.

Further analysis is presented in Figure 3, showing the modal energy sorting and modal extraction results for both TIC-DMD and SPDMD at different Reynolds numbers. The dominant modes extracted by both methods are consistent, indicating good agreement in capturing the main dynamic features. Among the seven modes extracted, three modes are identical for both methods. By comparing the modal energy distribution, the SPDMD shows a more dispersed modal energy distribution, with more significant differences in energy across modes, especially at Re = 2×10^6, where the modal energy proportion decreases in a stepwise fashion. In contrast, the TIC-DMD exhibits a higher concentration of dominant modal energy, with the extracted modes accounting for a larger proportion of the total modal energy, indicating that TIC-DMD prioritizes modes with larger energy contributions. At Re = 5×10^5, the dominant modes in TIC-DMD account for 12% of the total energy, while those in SPDMD account for only 3.2%. As the Reynolds number increases, at Re = 2×10^6, the dominant modal energy in TIC-DMD accounts for approximately 8.5%, while in SPDMD, the dominant modal energy accounts for only 2%. This trend suggests that the increasing complexity of high Reynolds number flow fields reduces the representativeness of dominant modes in capturing the overall flow field characteristics.

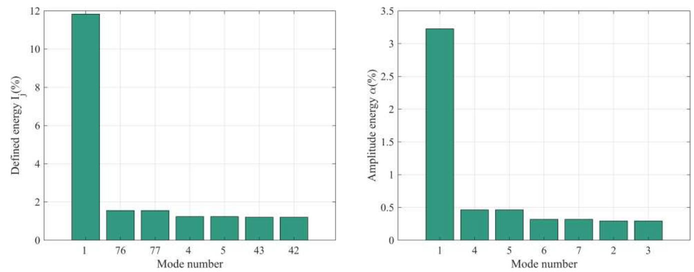

TIC-DMD SPDMD

(a) Re=5×10^5

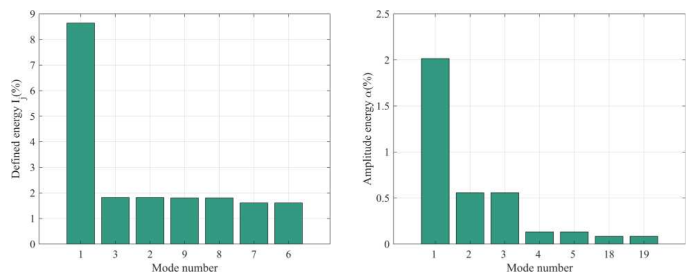

TIC-DMD SPDMD

(b) Re=2×10^6

Figure 3: Energy Sorting of seven Modes.

3.1.1 Analysis of the First-Order Modes

Figure 4 presents a comparison of the first-order modes in the U and V directions extracted using standard DMD, TIC-DMD, and SPDMD methods across different Reynolds numbers. The modal sorting in standard DMD primarily relies on initial energy or growth rates (such as initial amplitude sorting) (Chen et al., 2021). However, in high Reynolds number flows, the multi-scale characteristics of the flow field give rise to significant transient modes or noise interference. In the top lid-driven cavity flow at Re = 5×10^5 and Re = 2×10^6, the first-order modes extracted by standard DMD do not display the mean flow field with a frequency of 0, but rather show fragmented residual structures. This indicates that standard DMD is susceptible to high-frequency noise or secondary transient modes (Noack et al., 2016), failing to accurately capture the fundamental spatial characteristics of the flow field. Particularly at $Re = 2\times10^6$, the first-order mode from standard DMD exhibits more small-scale vortices and fragmented regions, reflecting its sensitivity to secondary dynamics rather than accurately capturing the main flow structure.

In contrast, TIC-DMD sorts modes by integrating the cumulative energy of each mode over the entire time domain, avoiding over-reliance on initial conditions (Arbabi et al., 2017). In the flow fields at $Re = 5\times10^5$ and $Re = 2\times10^6$, the first-order mode from TIC-DMD consistently represents a stable mean flow field (real part of the eigenvalue ≈ 1, imaginary part ≈ 0), and its spatial distribution shows smooth and stable patterns (see Figure 3). This mode accurately reflects the primary dynamic features of the flow field. Unlike standard DMD, TIC-DMD can overcome transient variations in the flow field, focusing on modes that describe the long-term behavior of the flow field, demonstrating strong robustness.

SPDMD optimizes the modal amplitude through sparsity constraints, suppressing noise and retaining key modes (Brunton et al., 2016). Its first-order mode is identical to that of TIC-DMD, further verifying the complementarity and robustness of the two methods in modal selection. SPDMD, while retaining the dominant modes, removes less important noise modes, especially in high-noise or highly complex flow fields, demonstrating higher computational efficiency and accuracy.

As the Reynolds number increases from 5×10^5 to 2×10^6, the flow field's nonlinearity increases, exhibiting more vortices and small-scale structures, which results in a more dispersed energy distribution (see Figure 4). The modes extracted by standard DMD under these conditions exhibit distinct "fragmentation" characteristics, indicating its difficulty in effectively distinguishing between dominant and secondary modes when handling high Reynolds number flows. In contrast, TIC-DMD and SPDMD are able to stably extract the first-order mode representing the mean flow field and preserve the main vortex structures in the flow field. At $Re = 5\times10^5$, the flow field is relatively smooth, and the first-order modes from TIC-DMD and SPDMD clearly display large-scale circulation structures, ensuring that the modes' physical meaning aligns with the true dynamics of the flow field. Although the flow field is more turbulent at $Re = 2\times10^6$, the first-order modes from TIC-DMD and SPDMD still effectively identify the dominant circulation, while the modes from standard DMD are overwhelmed by high-frequency noise and small vortices, failing to accurately reflect the primary features of the flow field.

Through global energy integration or sparsity constraints, TIC-DMD and SPDMD effectively filter out high-frequency noise and small-scale turbulence, focusing on the dominant modes, ensuring that the modes' physical meaning aligns with the true dynamics of the flow field. Taking $Re = 2\times10^6$ as an example, despite the presence of many fragmented regions in the flow field, the first-order modes from TIC-DMD and SPDMD still maintain spatial consistency, indicating that both methods exhibit high adaptability and precision for complex flows. With this optimized modal selection, TIC-DMD and SPDMD significantly reduce errors in flow field reconstruction, and their computational efficiency exceeds that of standard numerical simulations (Hu et al., 2023). Particularly, SPDMD enhances stability in high-noise environments through parameter optimization (Iwasaki et al., 2022), while TIC-DMD's global energy integration strategy further strengthens the reliability of modal selection. The optimized modal selection in both methods not only improves the accuracy of the analysis but also substantially reduces computation time, showing significant advantages, especially in high Reynolds numbers and complex flow field conditions.

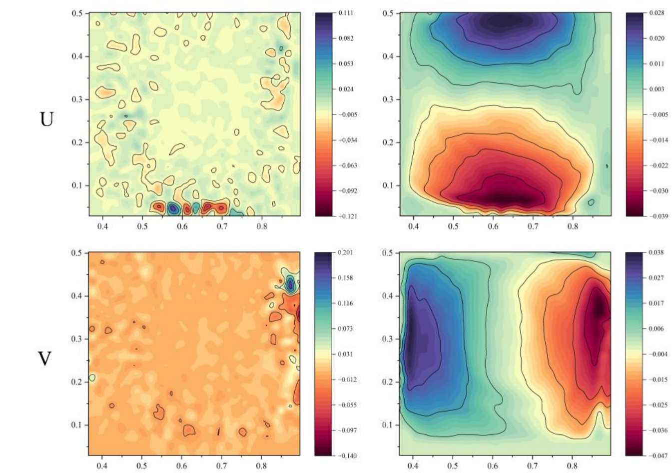

DMD TIC-DMD(SPDMD)

(a) Re=5×10^5

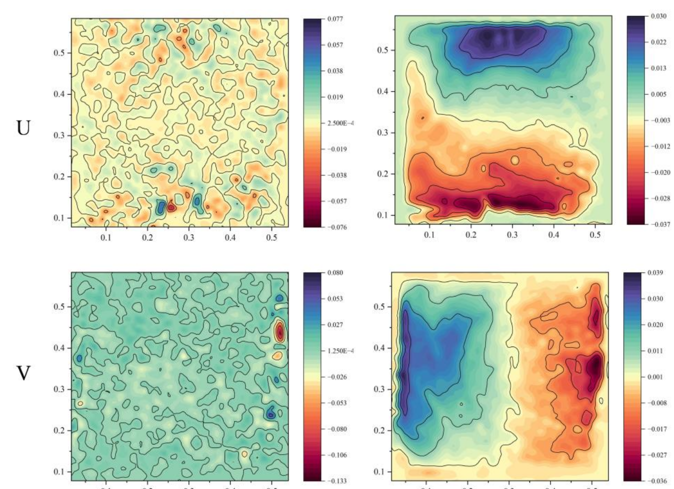

DMD TIC-DMD(SPDMD)

(b) Re=2×10^6

Figure 4: First-Order U-V Modes

3.2 Eigenvalue Spectrum

Figure 5 illustrates the eigenvalue spectrum analysis of standard DMD, TIC-DMD, and SPDMD at different Reynolds numbers. Eigenvalues inside the unit circle represent decaying modes, which have a certain impact on the early evolution of the flow field, but as time progresses, their structure gradually decays, reducing their influence on the flow field (Maziar et al., 2017). For example, at $Re = 5\times10^5$, the first few modes extracted by the standard DMD method exhibit significant high-frequency characteristics. Specifically, the first mode has a growth rate of -30.6315 and a frequency of 24.793 Hz, while the third mode has a growth rate of -30.7544 and a frequency of 49.370 Hz. These modes exhibit relatively high oscillation frequencies, with energy dissipating rapidly over a short time. However, in the fourth mode, standard DMD identifies a structure approaching steady state, with a decay rate of only -0.0127 and a frequency of 0 Hz. This suggests that the standard method has a noticeable lag in capturing steady-state structures (Ferrer et al., 2014).

In contrast, the TIC-DMD method, at $Re = 2\times10^6$, shows that the first mode exhibits low-frequency oscillatory characteristics, with a decay rate of only 0.0974 and a frequency of 0 Hz. This indicates that this mode corresponds to large-scale vortex structures and can significantly influence the system's evolution over an extended time scale. Its energy characteristics reflect a dynamic equilibrium, neither rapidly decaying nor rapidly diverging (Maziar et al., 2017).

The SPDMD method tends to select eigenvalues close to the unit circle, and as the sparsity regularization parameter increases, the number of selected eigenvalues gradually decreases. In the SPDMD results at $Re = 5\times10^5$, the second mode (decay rate of -0.0421, frequency of 0.515 Hz) and the fourth mode (decay rate of -0.5407, frequency of 1.4369 Hz) are both located near the unit circle, indicating the method's preference for stable modes. Notably, the clustering of feature value near the point (1, 0) suggests that SPDMD favors selecting steady-state structure modes. This characteristic becomes more pronounced at $Re = 2\times10^6$, where the first mode of SPDMD (decay rate of 0.0974, frequency of 0 Hz) is directly located at the (1, 0) point, accurately capturing the actual flow characteristics of the flow field.

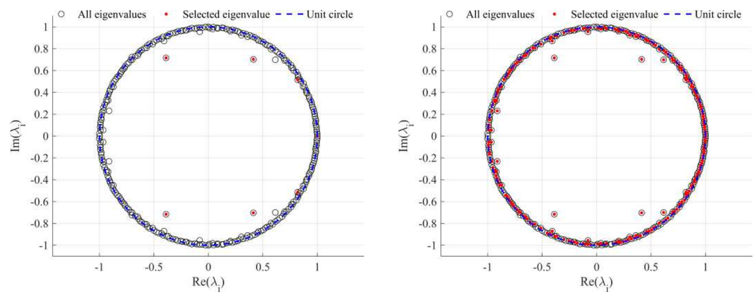

N=7 N=246

DMD

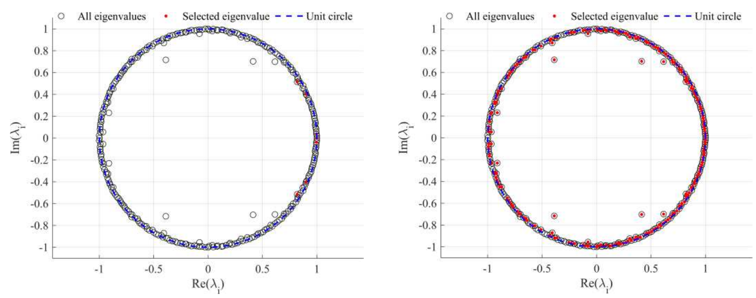

N=7 N=246

TIC-DMD

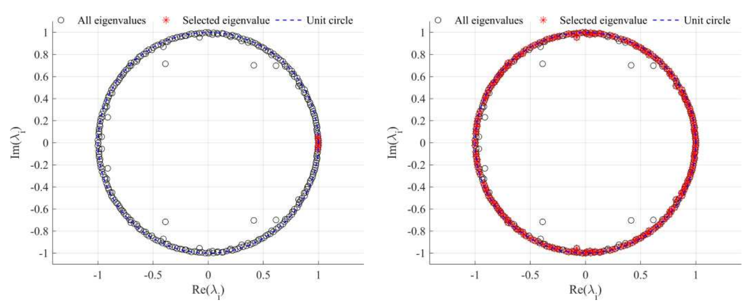

N=7 N=246

SPDMD

(a) Re=5×10^5

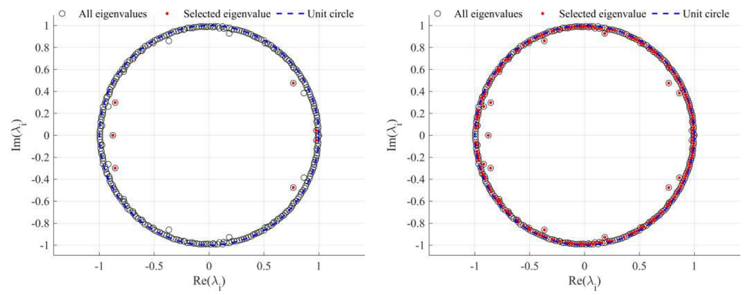

N=7 N=246

DMD

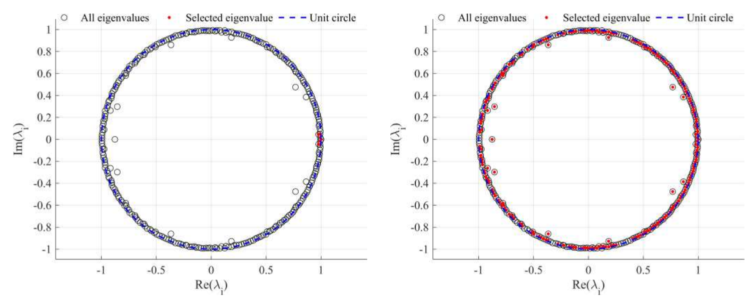

N=7 N=246

TIC-DMD

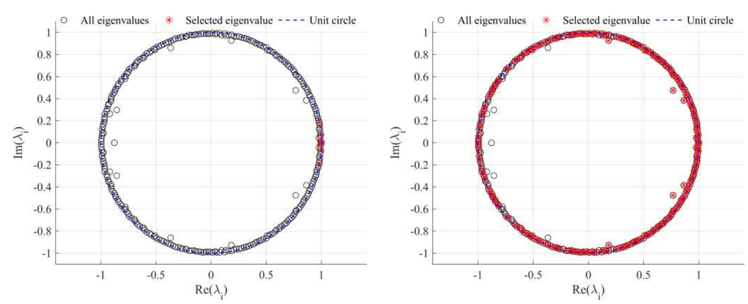

N=7 N=247

SPDMD

(b) *Re*=2×10^6

Figure 5 TIC-DMD - SPDMD Eigenvalue Spectrum.

3.3 Frequency-Energy Spectrum

Figure 6 shows the frequency-energy spectra for TIC-DMD and SPDMD methods at different Reynolds numbers. With N=7, the modal points selected by both TIC-DMD and SPDMD are mostly concentrated in the low-frequency region. At $Re = 5\times10^5$, TIC-DMD selects a broader frequency range, whereas at $Re = 2\times10^6$, SPDMD selects a wider frequency range. Additionally, there is a difference between the corrected amplitude and the original amplitude, indicating that SPDMD optimizes the modal amplitude through sparsity constraints, prioritizing modes that have a significant impact on the flow field evolution.

As the number of modes increases (N=246/247), the frequencies of the selected modes extend outward, which is consistent with the trend observed in the eigenvalue spectrum of TIC-DMD and SPDMD shown in Figure 5 (the eigenvalue points spread out along the x-axis), indicating a proportional relationship between the imaginary part of the eigenvalue and the frequency (ω) (see Equation 11).

TIC-DMD selects modes based on descending modal energy, starting with the mode that has the highest energy, ensuring a prioritized energy distribution. In contrast, SPDMD first optimizes modal selection through sparsity constraints and then sorts the corrected modal amplitudes (Jovanović et al., 2014). In SPDMD, the corrected amplitude energy may not necessarily be the highest, reflecting that SPDMD not only focuses on modes with the maximum amplitude but also identifies the modes that have the greatest impact on the time evolution of the data sequence (Erichson et al., 2019).

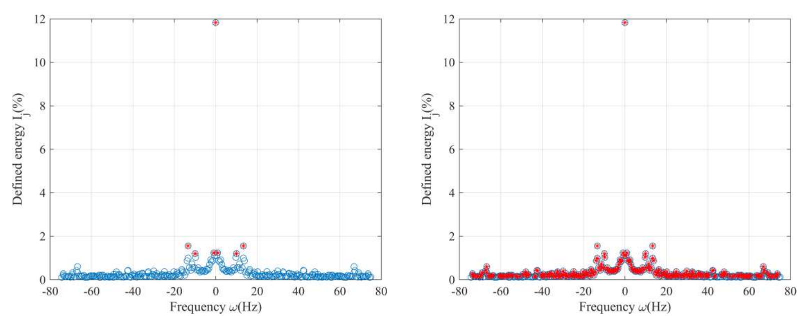

N=7 N=246

TIC-DMD

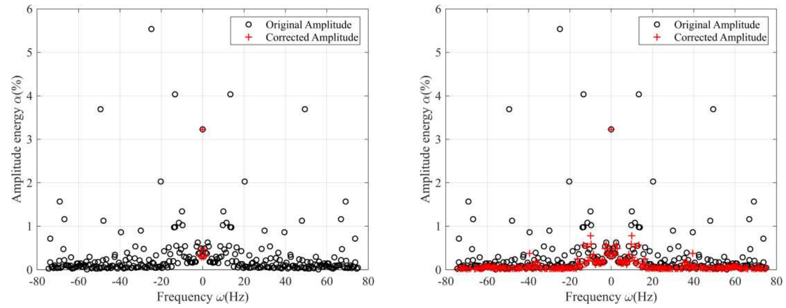

N=7 N=246

SPDMD

(a) *Re*=5×10^5

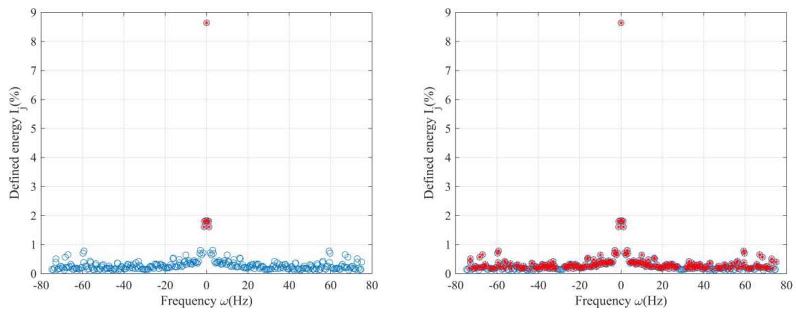

N=7 N=247

TIC-DMD

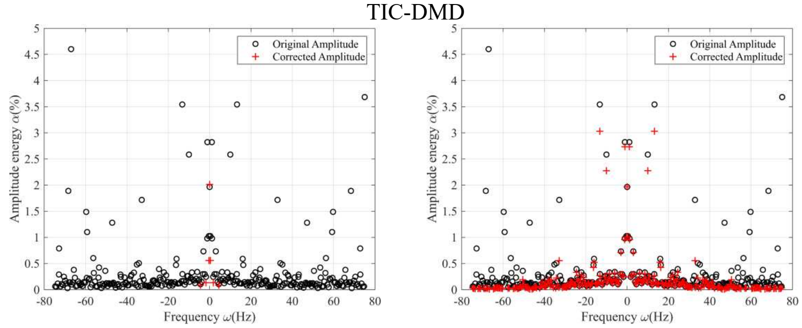

N=7 N=247

SPDMD

(b) *Re*=2×10^6

Figure 6 Frequency-Energy Plot

3.4 Evolution of the First Seven Modal Coefficients

To reveal the role of each mode in the development of the cavity flow, the modal coefficients are defined as (Rowley et al., 2017):

$$b_i = \alpha_i \exp\left\{\left[\ln(\lambda_i) / \Delta t\right] t\right\} \tag{30}$$

As shown in Figure 7, modes with a frequency of zero are omitted, as they represent the mean flow or steady-state structure of the flow field. Since the remaining modes are conjugate modes with negative growth rates, the amplitude of the modal coefficients gradually decreases over time. By examing the trend of the modal coefficients over time, it becomes clear that standard DMD always prioritizes modes with larger initial amplitudes during selecting modes. These modes, when N=7, rapidly decay at any Reynolds number, causing their impact on the flow field to diminish quickly over a short period. As the number of modes increases to 246 /247, additional modes that can persistently affect the flow field appear. This is due to the inclusion of more modes, enabling a more comprehensive capture of the flow field’s long-term dynamic features.

Although TIC-DMD also selects modes with larger initial amplitudes, which decay relatively quickly, it employs the Time Integration Contribution method to sort and select modes with low decay rates that have a lasting impact on the flow field. For example, at N=7, in the flow fields at Re=5×10^5 and Re=2×10^6, modes 4 and 5 (for Re=5×10^5) and modes 2 and 3 (for Re=2×10^6) exhibit slower decay and larger amplitudes, significantly influencing the flow field's evolution. Their energy contributions are just below that of the first-order mode, indicating their importance in the flow field.

In contrast, the SPDMD method, through sparsity constraints optimization, prioritizes modes with lower decay rates and suppresses rapidly decaying high-frequency modes. While SPDMD effectively retains low-frequency modes that exert a lasting influence on the flow field's evolution, these modes generally have smaller amplitudes. For example, at Re=2×10^6, the amplitudes of modes 2 and 3 selected by SPDMD are approximately 0.8, whereas the amplitudes of modes 2 and 3 in TIC-DMD are close to 1. Although these modes have a long-lasting effect, their lower amplitudes may lead to a smaller impact on the flow field.

Overall, as the number of modes increases, the standard DMD method primarily selects modes with larger initial amplitudes. Although these modes decay rapidly, they have a more significant impact on the flow field during the initial stages. TIC-DMD, in its selection process, includes both modes with large initial amplitudes and fast decay rates, as well as modes with slower decay rates that can sustain their influence. SPDMD, however, focuses more on selecting modes with slower decay rates and selects fewer modes with rapid decay. While TIC-DMD provides a more comprehensive modal selection, it is important to note that those modes with large initial values but fast decay, despite their short duration of influence, may still play a key role in ultra-high Reynolds number flow fields.

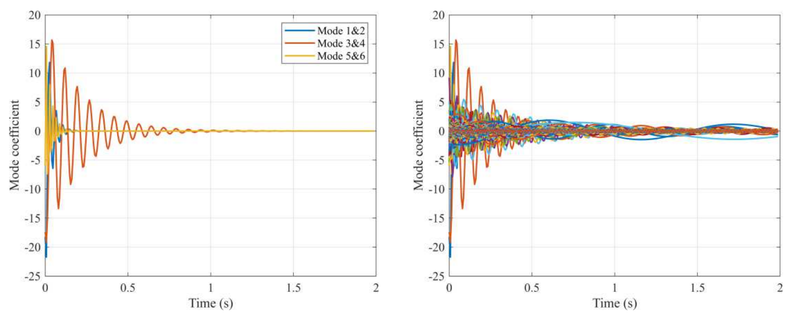

N=7 N=246

DMD

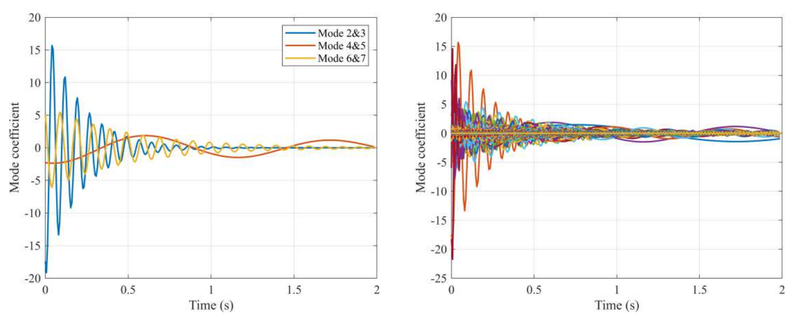

N=7 N=246

TIC-DMD

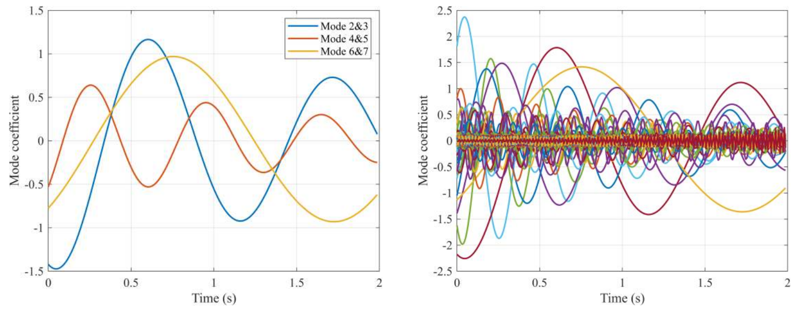

N=7 N=246

SPDMD

(a) $Re=5\times10^5$

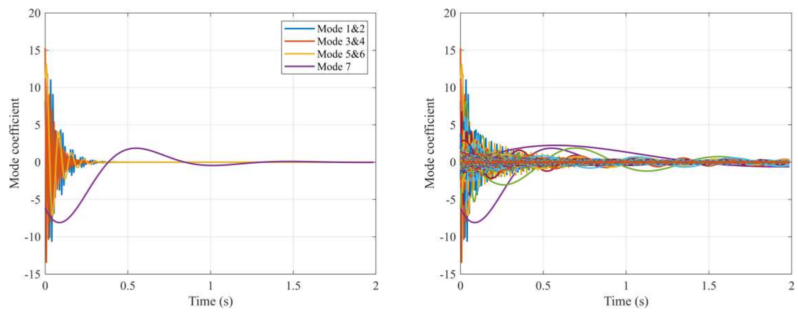

N=7 N=247

DMD

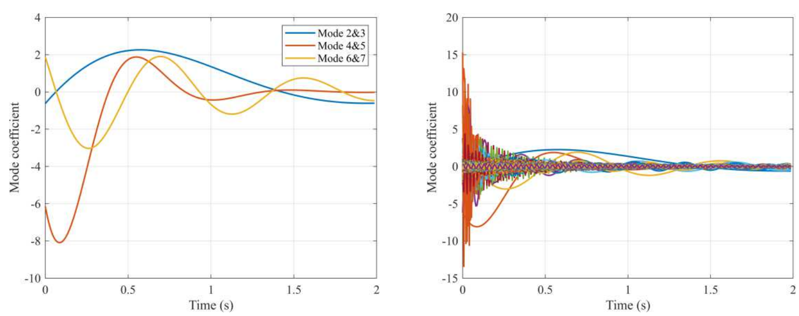

N=7 N=247

TIC-DMD

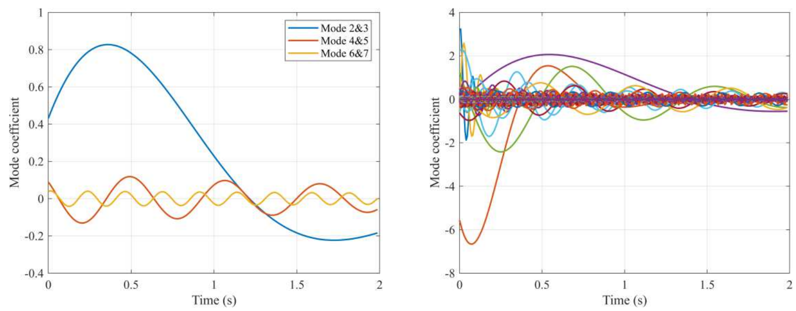

N=7 N=247

SPDMD

Re=2×10^6

Figure 7: Modal Coefficient Evolution.

3.5 Flow Field Reconstruction

To systematically evaluate the performance of DMD, TIC-DMD, and SPDMD methods in flow field reconstruction, this section reconstructs the flow field of the 120th snapshot using the 7th and 246th modes. Figure 8 presents the reconstruction characteristics of different methods at $Re = 5\times10^5$ and $Re = 2\times10^6$, including streamline distribution, total velocity distribution, and vortex structures. It can be observed that, at different Reynolds numbers and modal numbers, both TIC-DMD and SPDMD methods effectively capture the main morphological features of the actual flow field, including the general distribution of total velocity, the direction of streamline motion, and the location of vortices.

At $Re = 5\times10^5$, the 7th mode extracted by standard DMD fails to effectively reconstruct the meandering streamline shape, revealing its limitations at low modal numbers. In contrast, TIC-DMD and SPDMD are able to better capture the large-scale circulation structure. When $Re = 2\times10^6$, standard DMD fails to extract the dominant modes of the flow field, leading to significant differences between the reconstructed flow field and the actual flow field, failing to reflect the fundamental dynamic features of the flow. On the other hand, TIC-DMD and SPDMD are able to stably reconstruct the dominant circulation structures of the flow field, despite the flow being more turbulent.

Snapshot

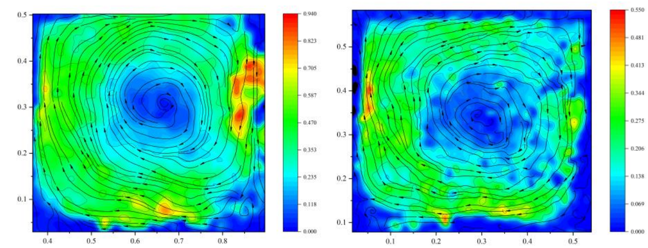

Re=5×10^5 Re=2×10^6

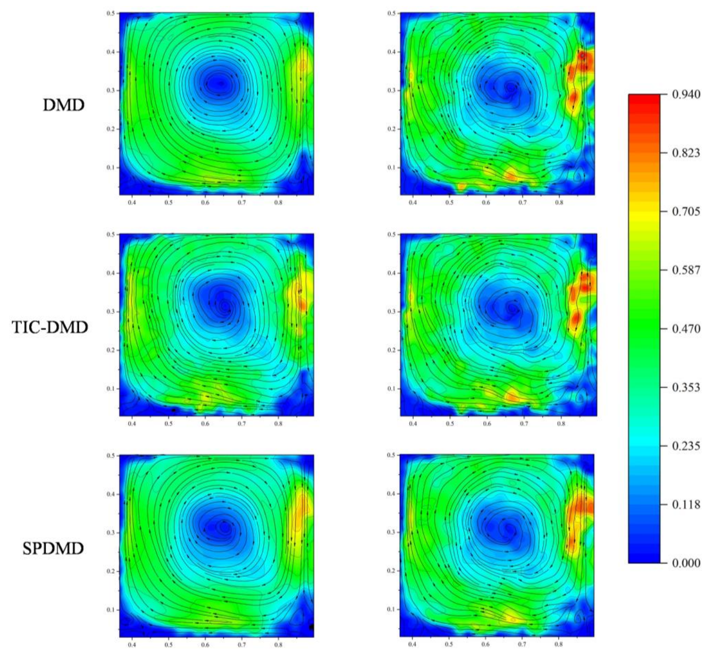

N=7 N=246 (247)

Re=5×10^5

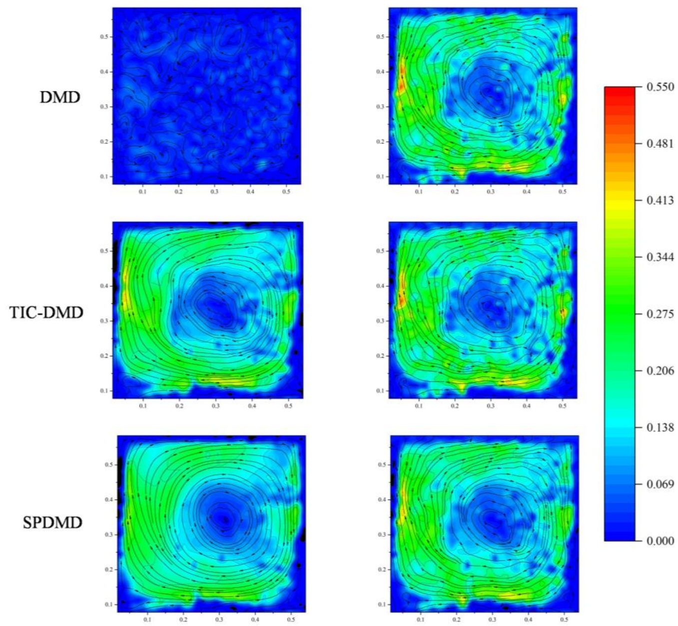

N=7 N=246 (247)

Re=2×10^6

Figure 8: Flow field reconstruction characteristics of DMD, TIC-DMD, and SPDMD methods at different Reynolds numbers.

To quantitatively evaluate the performance of the three methods in flow field reconstruction, the Relative L2 Error (RLE) of the 120th snapshot and the reconstruction errors of all snapshots are calculated. Tables 1 and 2 present the reconstruction errors for the 120th snapshot and for all snapshots, respectively. From the analysis, it can be seen that at low modal numbers (N=7), the reconstruction error of standard DMD is relatively large, especially at Re = 2×10^6, where the failure to effectively extract the dominant modes of the flow field leads to a significant increase in the reconstruction error. In contrast, TIC-DMD and SPDMD methods perform more stably at low modal numbers. At Re = 5×10^5, when reconstructing the 120th snapshot, the error for TIC-DMD is 0.2421, which, although higher than SPDMD (0.2151), is lower than that of standard DMD (0.2423), indicating that SPDMD is better at extracting the dominant features of the flow field.

At higher modal numbers (N=246/247), TIC-DMD shows a clear advantage. When $Re = 5\times10^5$ and reconstruction errors are calculated for all snapshots, SPDMD has a reconstruction error of 0.0449, while TIC-DMD's error is only 0.0175, a reduction of 61.02%. This further validates that TIC-DMD, through its global energy integration strategy, effectively filters noise and captures the dominant modes of the flow field. While SPDMD also shows some advantages at higher modal numbers, its reconstruction error is still significantly higher than TIC-DMD. Standard DMD shows the worst performance at low modal numbers, especially at $Re = 2\times10^6$, where it fails to extract the dominant modes of the flow field, resulting in a reconstruction error of 85.25%, much higher than TIC-DMD and SPDMD.

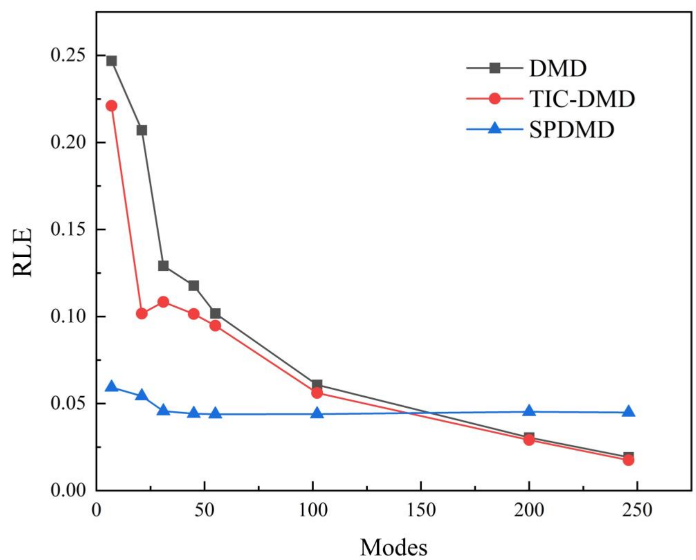

Figure 9: RLE of Each Mode for Different Reconstruction Methods

In summary, TIC-DMD demonstrates the best stability and accuracy in flow field reconstruction for high Reynolds number flows, particularly at higher modal numbers where reconstruction errors are minimized. SPDMD performs well at low modal numbers but does not match TIC-DMD at higher modal numbers, with its reconstruction error increasing significantly as the number of modes increases. Standard DMD performs the worst when reconstructing high Reynolds number flows at low modal numbers, as it fails to extract the dominant modes of the flow field, making it unsuitable for precise reconstruction of high Reynolds number flows.

Table 1: Reconstruction errors for the 120th snapshot at different modal numbers (a) *Re* = 5×10^5 (b) *Re* =2×10^6.

Modal Number	RLE(DMD)		RLE(TIC-DMD)		RLE(SPDMD)	
	(a)	(b)	(a)	(b)	(a)	(b)
246/247	0.0700	0.0894	0.0584	0.0835	0.1350	0.1389
7	0.2423	0.8804	0.2421	0.2161	0.2151	0.2700

Table 2: Reconstruction errors for all snapshots at different modal numbers (a) *Re* = 5×10^5 (b) *Re* = 2×10^6.

Modal Number	RLE(DMD)		RLE(TIC-DMD)		RLE(SPDMD)	
	(a)	(b)	(a)	(b)	(a)	(b)
246/247	0.0192	0.0206	0.0175	0.0227	0.0449	0.0374
7	0.2469	0.8525	0.2211	0.1062	0.0593	0.1272

To further evaluate the reconstruction performance of the DMD, TIC-DMD, and SPDMD methods in the time domain, this section also analyzes the velocity reconstruction at the same point across all time steps. Figure 10 presents the U-V velocity reconstruction results of DMD, TIC-DMD, and SPDMD methods at different modal numbers (N=7 and N=246/247) under the conditions of *Re* = 5×10^5 and *Re* = 2×10^6. The results show that at low modal numbers (N=7), TIC-DMD exhibits large variations in the reconstructed velocity at the initial stages, indicating that this method extracted modes with larger amplitudes and faster decay rates, leading to stronger fluctuations during the reconstruction process. In contrast, SPDMD provides a smoother velocity reconstruction. At $Re = 5\times10^5$, SPDMD has a reconstruction error of 0.6021 at low modal numbers, which is smaller than the error for TIC-DMD.

Table 3: Reconstruction errors for all time steps (a) $Re = 5\times10^5$ (b) $Re = 2\times10^6$.

Modal Number	RLE（DMD）		RLE（TIC-DMD）		RLE(SPDMD)	
	(a)	(b)	(a)	(b)	(a)	(b)
246/247	0.1931	0.3197	0.1433	0.3027	0.3443	0.5054
7	1.6385	2.8958	1.3658	0.7556	0.6133	0.6021

As the number of modes increases (N=246/247), TIC-DMD shows a significant improvement in reconstruction accuracy. At $Re = 5\times10^5$ the reconstruction error decreases to 0.1433, a 58.4% reduction compared to SPDMD (0.3443) and a 25.8% reduction compared to DMD (0.1931). This indicates that TIC-DMD is better at fitting the actual flow field and accurately capturing the dynamic characteristics of the flow at higher modal numbers. Notably, at $Re = 2\times10^6$, TIC-DMD's reconstruction error is 0.3027, which is substantially lower than SPDMD's 0.5054 and DMD's 0.3197, highlighting TIC-DMD's greater stability and smaller errors under high Reynolds number conditions.

In summary, TIC-DMD exhibits stronger adaptability at higher modal numbers, enabling more accurate capture of the dynamic characteristics of high Reynolds number flows. While SPDMD performs better at lower modal numbers, its accuracy decreases as the number of modes increases, failing to capture transient numerical modes as effectively as TIC-DMD.

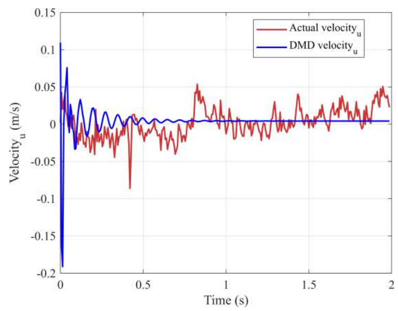

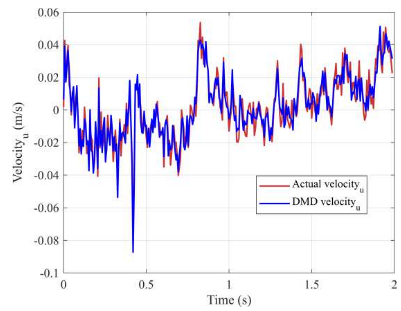

N=7 N=246

U-velocity

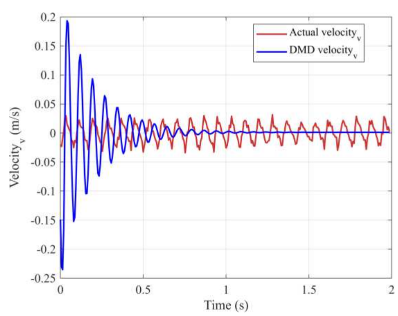

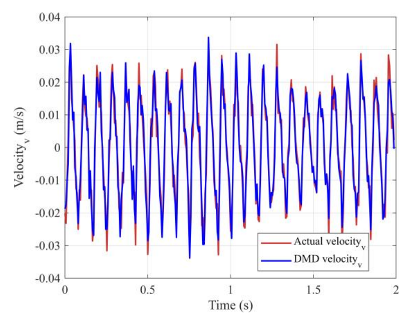

N=7 N=246

V-velocity

DMD

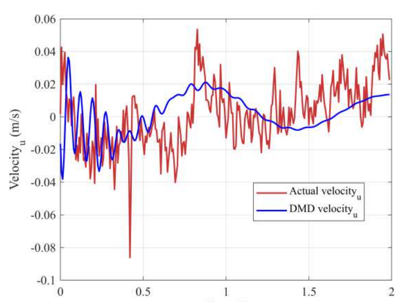

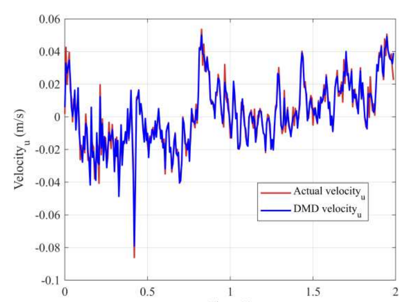

N=7 N=246

U-velocity

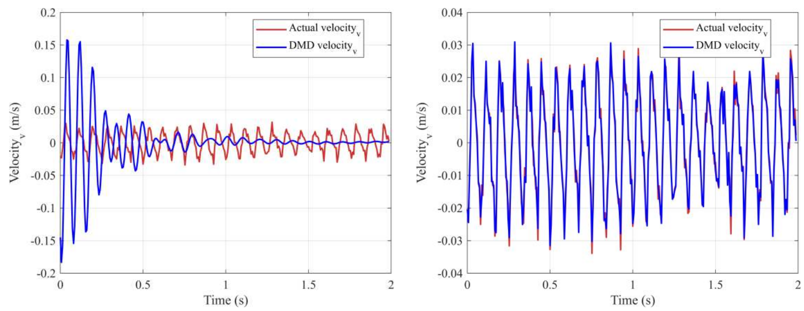

N=7 N=246

V-velocity

TIC-DMD

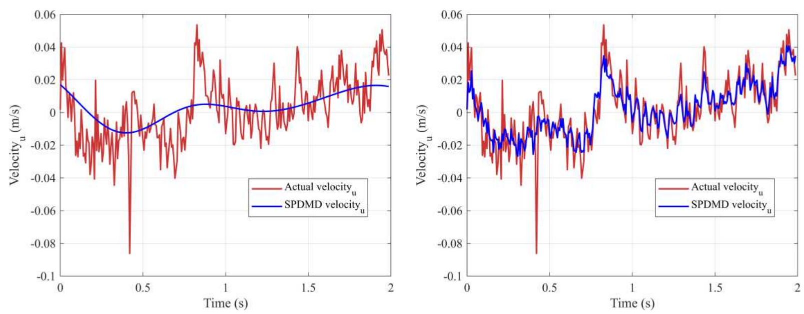

N=7 N=246

U-velocity

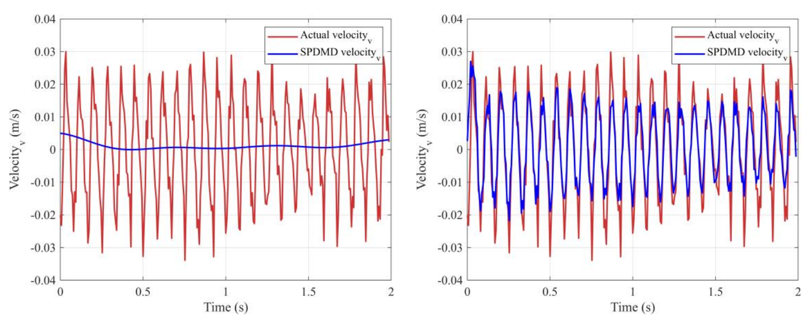

N=7 N=246

V-velocity

SPDMD

(a) Re=5×10^5

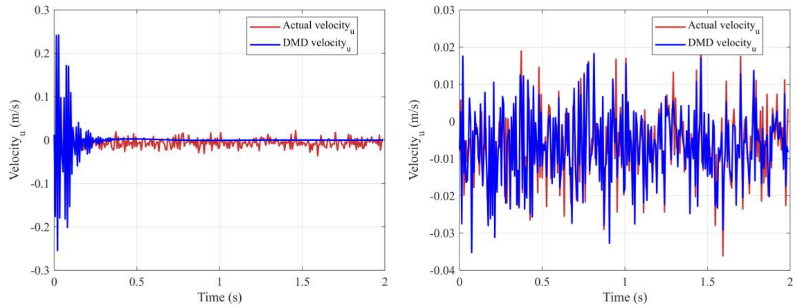

N=7 N=247

U-velocity

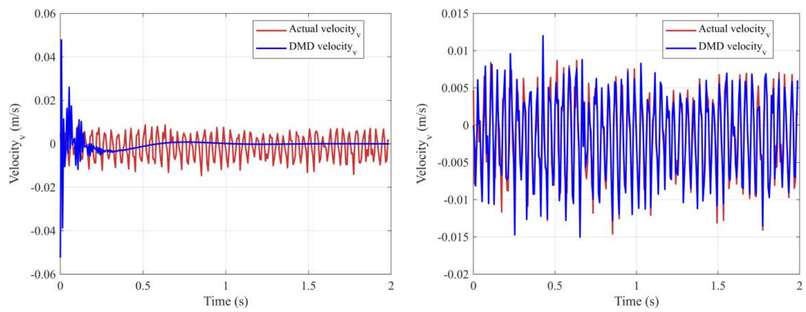

N=7 N=247

V-velocity

DMD

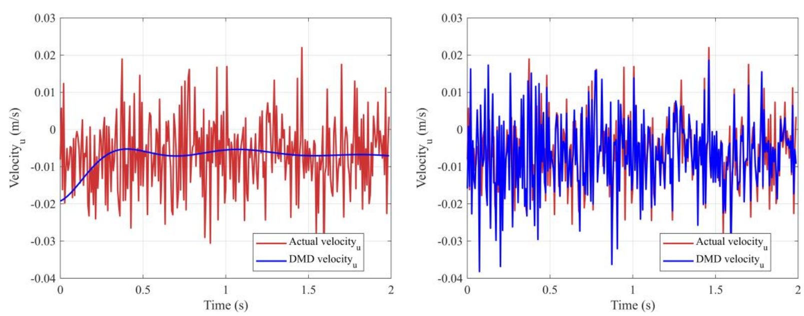

N=7 N=247

U-velocity

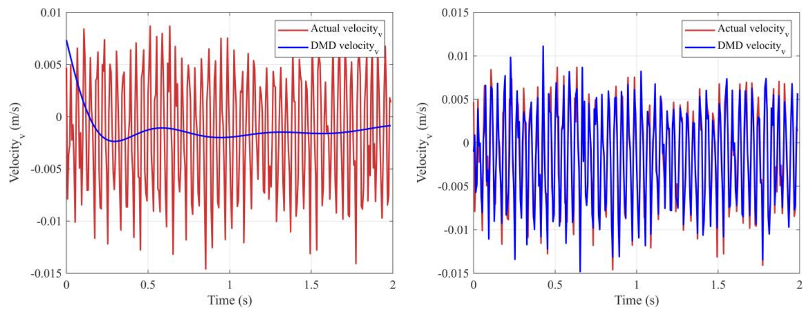

N=7 N=247

V-velocity

TIC-DMD

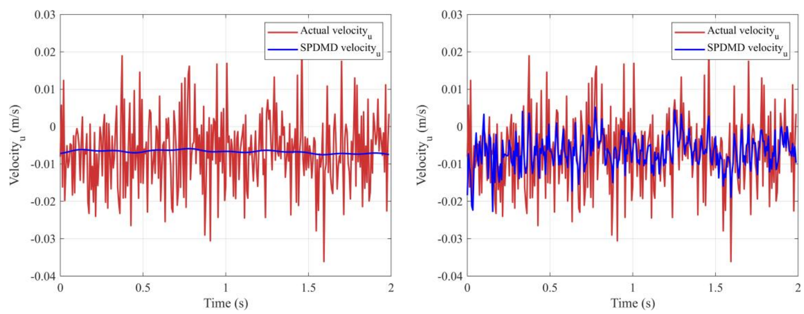

N=7 N=247

U-velocity

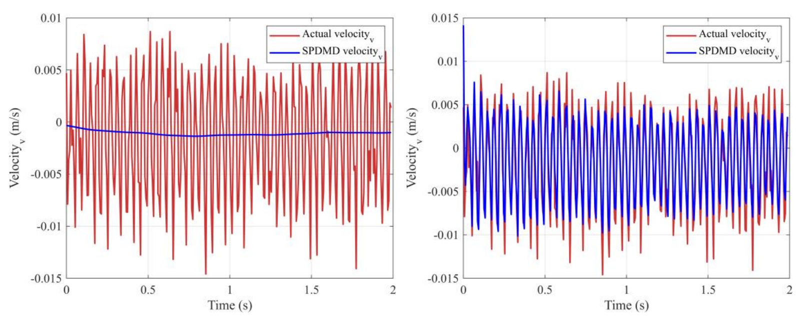

N=7 N=247

V-velocity

SPDMD

(b) $Re=1\times10^6$

Figure 10: U-V velocity reconstruction at a specific point in space.

5. Conclusion

This study examines the application of standard DMD, TIC-DMD, and SPDMD in high Reynolds number cavity flows, evaluating their performance in modal extraction, feature representation, and flow field reconstruction. Using PIV experimental data at Re = 5×10^5 and Re = 2×10^6, it assesses their strengths and limitations in capturing multi-scale turbulence dynamics.

TIC-DMD and SPDMD incorporate global energy integration and sparse optimization strategies, respectively, to effectively mitigate high-frequency noise and small-scale structures in high Reynolds number flows. This enhances the accuracy and reliability of flow field analysis. In the top cover cavity-driven flow at Re = 2×10^6, both methods accurately identify the dominant circulation structure, whereas standard DMD struggles to represent the primary dynamic features of the flow.

At high Reynolds numbers, TIC-DMD and SPDMD improve the accuracy of dynamic flow field analysis through optimized modal selection. At Re = 5×10^5, the initial modes extracted by standard DMD show significant high-frequency characteristics, leading to rapid energy dissipation. At Re = 2×10^6, standard DMD delayed the extraction of steady-state structures. In contrast, TIC-DMD effectively captures low-frequency large vortex structures at Re = 2×10^6, while SPDMD ensures more stable decay rates and frequencies at Re = 5×10^5.

In terms of performance, TIC-DMD excels at higher modal numbers (N = 246), achieving a reconstruction error of RLE = 0.0175 at Re = 5×10^5 that is 61.02% lower than SPDMD. SPDMD outperforms at lower modal numbers (N = 7) with an RLE = 0.1272 at Re = 2×10^6, but its performance deteriorates as the number of modes increases. In contrast, standard DMD shows high reconstruction errors at lower modal numbers (RLE = 0.8525 at Re = 2×10^6).

The modal sorting strategy presented in this study provides a novel approach for reduced-order modeling of high-dimensional nonlinear systems. Future work could explore hybrid methods, such as TIC-SPDMD, which combine global energy integration with sparse constraints to enhance the accuracy of modeling high-Reynolds-number flows in aerospace applications, such as supersonic jet screech analysis and turbulent wake dynamics. In conclusion, TIC-DMD and SPDMD highlights the advantages of global energy integration and sparse optimization. TIC-DMD is suitable for multi-scale turbulence analysis, while SPDMD is beneficial for real-time flow field control. The findings deepen our understanding of high Reynolds number flow dynamics and provides a solid foundation for modeling and optimizing complex flow fields.

Acknowledgements

This study is supported by the Qin Chuang Yuan high-level innovation and entrepreneurship talent project (No: QCYRCXM2023-099), the 2024 major projects to prevent and control sand demonstration 'Unveiled Marshal' project from the Inner Mongolia Department of Science and Technology (No: 2024JBGS0016), the National Foreign Experts Individual Program (Category H) under national funding (No: H20240398) , and the Xianyang Science and Technology Bureau (No: L2024-ZDYF-ZDYF-SF-0042).

References

Abu Seena, & Sung, H. J. (2011). Dynamic mode decomposition of turbulent cavity flows for self-sustained oscillations. International Journal of Heat and Fluid Flow, 32(6), 1098-1110. Doi:10.1016/j.ijheatfluidflow.2011.09.008.

Arai, Y., Muramatsu, S., Yasuda, H., Hayasaka, K., & Otake, Y. (2021). Sparse-coded dynamic mode decomposition on graph for prediction of river water level distribution. *ICASSP 2021 - 2021 IEEE International Conference on Acoustics, Speech and Signal Processing (ICASSP)*, Toronto, ON, Canada, 3225-3229. Doi:10.1109/ICASSP39728.2021.9414533.

Asada, H., & Kawai, S. (2025). Exact parallelized dynamic mode decomposition with Hankel matrix for large-scale flow data. *Theoretical and Computational Fluid*

Dynamics, 39(8). Doi:10.1007/s00162-024-00730-0.

Arbabi, H., & Mezić, I. (2017). Study of dynamics in post-transient flows using Koopman mode decomposition. *Physical Review Fluids*, 2(12), 124402. Do:10.1103/PhysRevFluids.2.124402.

Baars, W. J., Hutchins, N., & Marusic, I. (2017). Reynolds number trend of hierarchies and scale interactions in turbulent boundary layers. *Philosophical Transactions of the Royal Society A: Mathematical, Physical and Engineering Sciences, 375*(2089), 20160077. Doi:10.1098/rsta.2016.0077.

Brunton, S. L., Proctor, J. L., & Kutz, J. N. (2016). Discovering governing equations from data by sparse identification of nonlinear dynamical systems. *Proceedings of the National Academy of Sciences, 113*(15), 3932-3937.Doi:10.1073/pnas.1517384113.

Brunton, S. L., Noack, B. R., & Koumoutsakos, P. (2020). Machine learning for fluid mechanics. *Annual Review of Fluid Mechanics, 52*(1), 477-508. Doi:10.1146/annurev-fluid-010719-060214.

Burggraf, O. R. (1966). Analytical and numerical studies of the structure of steady separated flows. *Journal of Fluid Mechanics, 24*(1), 113-151. Doi:10.1017/S0022112066000324.

Chávez-Dorado, R., et al. (2025). Wave and turbulence separation using dynamic mode decomposition. *Ocean Engineering, 270*, 113672. Doi: 10.1016/j.oceaneng.2025.113672.

Chen, D., et al. (2024). Evolution analysis of cavitated water jet flow using DMD. *Physics of Fluids, 36*(5), 50123. Doi:10.1063/5.0024531.

Chen, K. K., Tu, J. H., & Rowley, C. W. (2012). Variants of dynamic mode decomposition: Boundary condition, Koopman, and Fourier analyses. *Journal of Nonlinear Science, 22*(6), 887-915. Doi:10.1007/s00332-012-9135-4.

Eckstein, A., & Vlachos, P. P. (2009). Digital particle image velocimetry (DPIV) robust phase correlation. *Measurement Science and Technology*, 20(5), 055401. Doi:10.1088/0957-0233/20/5/055401.

Erichson, N. B., Mathelin, L., Kutz, J. N., & Brunton, S. L. (2019). Randomized dynamic mode decomposition. *SIAM Journal on Applied Dynamical Systems, 18*(4), 1867-1891. Doi:10.1137/18M1215013

Chen, H., Zhong, Q., Wang, X. K., et al. (2014). Reynolds number dependence of flow past a shallow open cavity. *Science China Technological Sciences, 57*, 2161-2171. Doi:10.1007/s11431-014-5485-0.

Feldhusen-Hoffmann, A., Lagemann, C., Loosen, S., et al. (2021). Analysis of transonic buffet using dynamic mode decomposition. *Experimental Fluids, 62*(66). Doi:10.1007/s00348-020-03111-5.Gosea, I. V., & Pontes Duff, I. (2021). Toward Fitting Structured Nonlinear Systems by Means of Dynamic Mode Decomposition. International Series of Numerical Mathematics, 171, 53–74. Doi: 10.1007/978-3-030-72983-7_3.

Green, M. A., Rowley, C. W., & Haller, G. (2020). Detecting coherent structures in turbulent flows via machine learning. *Physics of Fluids, 32*(12), 125117. Doi: 10.1063/5.0030692.

Hu, C., Zheng, M., & Yang, C. (2023). Multilevel method for predicting flow fields in radial turbines based on SPDMD. *Journal of Numerical Methods for Heat and Fluid Flow*. Doi:10.1108/JNM-05-2023-0423.

Iwasaki, Y., Nonomura, T., Nakai, K., & Nagata, T. (2022). Evaluation of optimization algorithms and noise robustness of SPDMD. *IEEE Transactions on Control Systems Technology*. Doi:10.1109/TCST.2022.3140029.

Jovanović, M. R., Schmid, P. J., & Nichols, J. W. (2014). Sparsity-promoting dynamic mode decomposition. *Physics of Fluids, 26*(2), 024103. Doi:10.1063/1.4866891.

Peng, J., Gao, L., Yu, X., Qin, F., Liu, B., Cao, Z., Wu, G., & Han, M. (2022). Combustion oscillation characteristics of a supersonic ethylene jet flame using high-speed planar laser-induced fluorescence and dynamic mode decomposition. *Energy*, 239(Part D), 122330. Doi:10.1016/j.energy.2021.122330.

Haller, G. (2015). Lagrangian coherent structures. *Annual Review of Fluid Mechanics, 47*(1), 137–162. Doi:10.1146/annurev-fluid-010313-141322.

Hemati, M. S., Williams, M. O., & Rowley, C. W. (2017). Dynamic mode decomposition for large and streaming datasets. *AIAA Journal, 55*(4), 401–421. Doi:10.2514/1.J055499.

Kong, X., Li, C., Wang, C., Zhang, Y., & Zhang, J. (2020). Short-term electrical load forecasting based on error correction using dynamic mode decomposition. *Applied Energy, 261*, 114368. Doi:10.1016/j.apenergy.2019.114368.

Kou, J., & Zhang, W. (2016). An improved criterion to select dominant modes from dynamic mode decomposition. *European Journal of Mechanics B/Fluids*, 62, 109–129. Doi:10.1016/j.euromechflu.2016.11.015.

Kutz, J.N., Brunton, S.L., Brunton, B.W., & Proctor, J.L. (2016). Dynamic Mode Decomposition: Data-Driven Modeling of Complex Systems. SIAM.

Le Clainche, S., Vega, J. M., & Soria, J. (2017). Higher order dynamic mode decomposition of noisy experimental data: The flow structure of a zero-net-mass-flux jet. *Experimental Thermal and Fluid Science, 88*, 336-353. Doi:10.1016/j.expthermflusci.2017.06.011

Li, Z., Zhou, J., Zhu, X., Zhou, J., & Pan, T. (2024). Investigation of Reynolds number effects on flow stability of a transonic compressor using a dynamic mode decomposition method. *Aerospace Science and Technology*, 124, 107247.Doi: 10.1016/j.ast.20 24.109421.

Li, H., Fernex, D., Semaan, R., Tan, J., Morzyński, M., & Noack, B. R. (2021). Cluster-based network model. *Journal of Fluid Mechanics, 906*, A21. Doi:10.1017/jfm.2020.785.

Li, X., Zhang, Q., & Huang, W. (2022). Sparse DMD-accelerated optimization of turbine blade cooling channels. *ASME Journal of Turbomachinery, 144*(11), 111009. Doi:10.1115/1.4055463.

Liao, Z.-M., Zhao, Z., Hemati, L.-B., Wan, Z.-H., Liu, N.-S., & Lu, X.-Y. (2023). Reduced-order variational mode decomposition to reveal transient and non-stationary dynamics in fluid flows. *Journal of Fluid Mechanics*, 966:A7. Doi:10.48550/arXiv.2209.12437.

Nguyen, D. B., Wu, P., Monico, R. O., & Chen, G. (2023). Dynamic mode decomposition for large-scale coherent structure extraction in shear flows. *IEEE Transactions on Visualization and Computer Graphics*, 29(2), 1531–1544. Doi:10.1109/TVCG.2021.3124729.

Koseff, J. R., & Street, R. L. (1984). The Lid-Driven Cavity Flow: A Synthesis of Qualitative and Quantitative Observations. *ASME Journal of Fluids Engineering, 106*(4), 390–398. doi:10.1115/1.3243136.

Marensi, E., Yalnız, G., Hof, B., & Budanur, N.B. (2023). Symmetry-reduced dynamic mode decomposition of near-wall turbulence. *Journal of Fluid Mechanics*, 954:A10. Doi:10.1017/jfm.2022.1001.

Menon, K., & Mittal, R. (2020). Dynamic mode decomposition-based analysis of flow over a sinusoidally pitching airfoil. *Journal of Fluids and Structures*, 94, 102886.Doi:10.1016/j.jfluid structs.2020.102886.

Liu, M., Tan, L., & Cao, S. (2020). Method of dynamic mode decomposition and reconstruction with application to a three-stage multiphase pump. *Energy*, 208, 118343. Doi:10.1016/j.energy.2020.118343.

Mohan, N., Soman, K. P., & Kumar, S. S. (2018). A data-driven strategy for short-term electric load forecasting using dynamic mode decomposition model. *Applied Energy, 232*, 229-244. doi:10.1016/j.apenergy.2018.09.190.

Noack, B. R., Stankiewicz, W., Morzyński, M., & Schmid, P. J. (2016). Recursive dynamic mode decomposition of transient and post-transient wake flows. *Journal of Fluid Mechanics*, 809, 843-872. Doi:10.1017/jfm.2016.583.

Page, J., & Kerswell, R.R. (2020). Searching turbulence for periodic orbits with dynamic mode decomposition. *Journal of Fluid Mechanics*, 886:A28.DOI: 10.1017/jfm.2019.1074.

Pasquariello, V., Hickel, S., & Adams, N.A. (2017). Unsteady effects of strong shock-wave/boundary-layer interaction at high Reynolds number. *Journal of Fluid Mechanics*, 823, 617–657. DOI:10.1017/jfm.2017.308.

Rowley, C.W. & Dawson, S.T.M. 2017. Model reduction for flow analysis and control. *Annual Review of Fluid Mechanics*, 49, 387-417.Doi:10.1146/annurev-fluid-010816-

060042.

Rowley, C. W., Mezić, I., Bagheri, S., Schlatter, P., & Henningson, D. S. (2009). Spectral analysis of nonlinear flows. *Journal of Fluid Mechanics, 641*, 115-127. Doi:10.1017/S0022112009992059.

Roy, R., & Gupta, A. K. (2023). Performance enhancement of swirl-assisted distributed combustion with hydrogen-enriched methane. *Applied Energy, 338*, 120919. doi:10.1016/j.apenergy.2023.120919.

Schmid, P. J. (2010). Dynamic mode decomposition of numerical and experimental data. *Journal of Fluid Mechanics, 656*, 5-28. Doi:10.1017/S0022112010001217.

Schmid, P. J. (2022). Dynamic mode decomposition and its variants. *Annual Review of Fluid Mechanics, 54*(1), 225–254. Doi:10.1146/annurev-fluid-030121-015835.

Schmid, P. J. (2023). The Dynamic Mode Decomposition: From Koopman Theory to Applications. In Mendez, M. A., Ianiro, A., Noack, B. R., & Brunton, S. L. (Eds.), *Data-Driven Fluid Mechanics: Combining First Principles and Machine Learning*. Cambridge University Press, 133-152. DOI:10.1017/9781108896214.012.

Smits, A. J., McKeon, B. J., & Marusic, I. (2021). High Reynolds number wall turbulence. *Annual Review of Fluid Mechanics, 53*(1), 353–387. Doi:10.1146/annurev-fluid-071320-095058.

Taira, K., Brunton, S. L., & Dawson, S. T. M. (2017). Modal analysis of fluid flows: An overview. *AIAA Journal, 55*(12), 4013–4041. Doi:10.2514/1.J056060.

Tanase, N.-O., Simionescu, S.-M., Broboana, D., & Balan, C. (2017). Experimental and numerical studies of the cavity flows at low Reynolds numbers. *Energy Procedia*, 210–216. Doi:10.1016/j.egypro.2017.03.1086.

Tiziano, P., Francesco, G., Francesco, S., et al. (2022). Proper orthogonal decomposition, dynamic mode decomposition, wavelet and cross wavelet analysis of a sloshing flow. *Journal of Fluids and Structures*, 112. DOI: 10.1016/j.jfluidstructs.2022.103676.

Tsolovikos, A., Bakolas, E., et al. (2020). Estimation and control of fluid flows using SPDMD. *IEEE Control Systems Letters*, 4(6), 1420–1425. **DOI:** 10.1109/LCSYS.202

0.3015776.

Wang, Z., Li, J., & Liu, H. (2022). Dynamic wind turbine wake reconstruction: A Koopman-linear flow estimator. *Energy*, 238, Part B, 121723. Doi:10.1016/j.energy.2021.121723.

Wang, P., Peng, Y., Cheng, S., Gao, L., Yin, X., Shen, Y., & Gao, X. (2025). Cavity flows at high Reynolds numbers. Physics of Fluids, 37(3), 035146. Doi:10.1063/5.0256965.

Ye, K., Wu, J., Ye, Z., et al. (2017). Dynamic mode decomposition and proper orthogonal decomposition analysis of the stability of flow past a cylinder. *Journal of Northwestern Polytechnical University*, 35(4), 599–607. doi:10.1016/j.jfluidstructs.2022.103603.

Zhang, H., Wang, L., et al. (2023). Sparsity promoting dynamic mode decomposition for data-driven modeling of wind turbine wake. *Energy*, 254, 124785. Doi:10.1088/1742-6596/2474/1/012028.